Tomography of Materials and Structures 2 (2023) 100011

Contents lists available at ScienceDirect

Tomography of Materials and Structures

journal homepage: www.journals.elsevier.com/tomography-of-materials-and-structures

Noise and blur removal from corrupted X-ray computed tomography scans: A multilevel and multiscale deep convolutional framework approach with synthetic training data (BAM SynthCOND)

Athanasios Tsamos[a,*], Sergei Evsevleev[a], Giovanni Bruno[a,b]

[a] Bundesanstalt für Materialforschung und-prüfung, Unter den Eichen 87, 12205 Berlin, Germany
[b] Institute of Physics and Astronomy, University of Potsdam, Karl-Liebknecht-Str. 24–26, 14476 Potsdam, Germany

ARTICLE INFO

Keywords:
XCT Data Conditioning
Denoising Deblurring Sharpening
Deep Convolutional Neural Network (DCNN)
In-Situ Computed Tomography
Metal Matrix Composite (MMC)
Synthetic Training Data
ACEnet

ABSTRACT

Regardless of the experimental care practiced in acquiring X-ray computed tomography (XCT) data, artifacts might still exist, such as noise and blur. This is typical for fast XCT data acquisitions (e.g., in-situ investigations), or low-dose XCT. Such artifacts can complicate subsequent analysis of the data. Digital filters can moderately cure extensive artifacts. The selection of filter type, intensity, and order of application is not always straightforward. To tackle these problems, a complete sequential multilevel, multi-scale framework: BAM SynthCOND, employing newly designed deep convolutional neural networks (DCNNs), was formulated. Although data conditioning with neural networks is not uncommon, the main complication is that completely artifact-free XCT data for training do not exist. Thus, training data were acquired from an in-house developed library (BAM SynthMAT) capable of generating synthetic XCT material microstructures. Some novel DCNN architectures were introduced (2D/3D ACEnet_Denoise, 2D/3D ACEnet_Deblur) along with the concept of Assertive Contrast Enhancement (ACE) training, which boosts the performance of neural networks trained with continuous loss functions. The proposed methodology accomplished very good generalization from low resemblance synthetic training data. Indeed, denoising, sharpening (deblurring), and even ring artifact removal performance were achieved on experimental post-CT scans of challenging multiphase Al-Si Metal Matrix Composite (MMC) microstructures. The conditioning efficiencies were: 92% for combined denoising/sharpening, 99% for standalone denoising, and 95% for standalone sharpening. The results proved to be independent of the artifact intensity. We believe that the novel concepts and methodology developed in this work can be directly applied on the CT projections prior to reconstruction, or easily be extended to other imaging techniques such as: Microscopy, Neutron Tomography, Ultrasonics, etc.

1. Introduction

1.1. Background and motivation

Quantitative analysis of X-ray Computed Tomography (XCT) data can be challenging due to post-reconstruction artifacts, such as noise, blur, streaking, and ring artifacts [1–4]. Typically, the correction of such artifacts is a tradeoff between resulting noise, blurring, low contrast at interfaces, and spatial resolution [2,5]. The problem is more apparent when the number of projections is limited, or some projections are corrupted. It becomes even more challenging if one does not have the possibility to repeat the experiment/measurement or if the original projections are missing. All the above cases are highly probable in the case of in-situ investigations, where XCT projections are acquired faster than usual, due to sampling requirements, which can lead to photon starvation [1–3]. Thus, a final reconstruction of low quality is to be expected [5,6]. Standard digital filters such as the Mean, the Gaussian, and the Median filters are inefficient for highly corrupted data. In such cases, their application can result in structural losses and edge suppression [4,6]. This loss of information occurs both when applied on the sinograms and directly on the reconstructions (e.g., smearing out of finer details occurs due to excessive smoothing). Various other more sophisticated adaptive filtering algorithms for noise reduction have been proposed and used over the years [1–3,5–8], paired with the conventional Filtered Back-Projection (FBP) method. For the task of ring artifact and stripe removal, various Fourier filters and wavelets

* Corresponding author.
E-mail address: athanasios.tsamos@bam.de (A. Tsamos).

https://doi.org/10.1016/j.tmater.2023.100011
Received 20 December 2022; Received in revised form 19 June 2023; Accepted 25 June 2023
Available online 29 June 2023

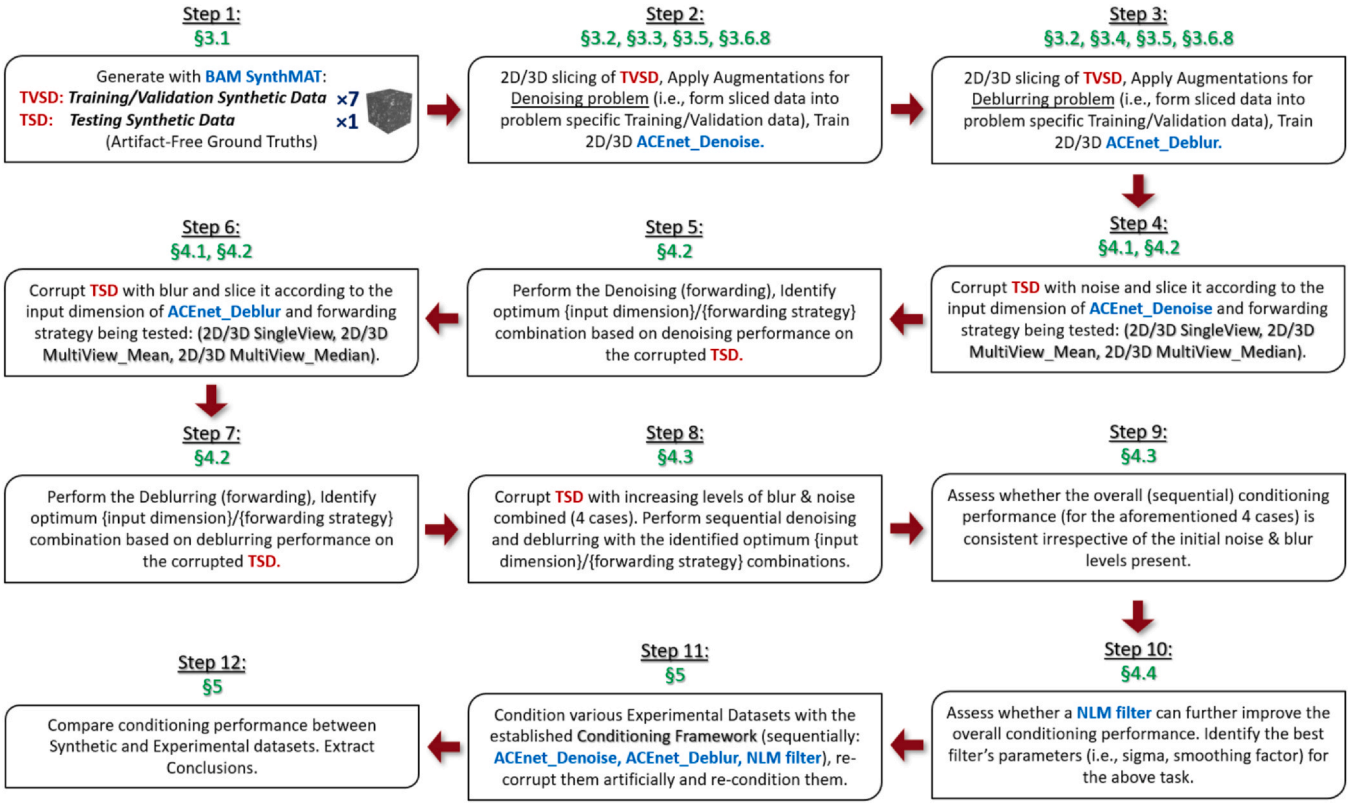

Fig. 1. Research Approach Pipeline and respective sections for each step.

have also been employed [4,9–11]. However, all the above filters have limitations: a precise edge restoration on highly corrupted datasets is a major challenge. Furthermore, wavelets are not universally applicable and typically require fine-tuning. More recently, some of the above barriers have been practically removed with the application of iterative reconstruction algorithms as an alternative to FBP. An example of this can be found in the works of Magkos et al. (DIRECTT reconstruction algorithm) in [12,13]. As it was shown, cone-beam artifacts can significantly be suppressed, even when fewer projections are available. A higher reconstruction quality can be achieved compared to the standard FBP, at the expense of computational effort and time. Iterative algorithms have the same limitations, as they cannot regenerate lost structural information in highly corrupted data. On the other hand, deep neural networks possess regenerative capabilities. Furthermore, they can generalize well in image conditioning if properly trained. Such training does not even require fine-tuning based on a certain artifact intensity (or orientation). The exploitation of artificial neural networks, and more specifically Deep Convolutional Neural Networks (DCNNs) (which are superb in image analysis), to tackle XCT data conditioning problems is not novel. In the past decade, they have extensively been used for Low-Dose XCT (LDXCT) data conditioning (but mostly in the medical sector). An excellent review on the subject by Kulathilake et al. can be found in [14], in which various artificial intelligence-based techniques are presented for XCT data conditioning (i.e., denoising, deblurring, etc.) As it was concluded, the major issue in both supervised and unsupervised approaches is the acquisition of artifact-free data for training. Typically, these come from Normal Dose XCT Data (NDXCT) [15], which still contain some artifacts. Furthermore, selecting suitable training datasets is a tough and highly empirical challenge as datasets are rarely interchangeable. Lastly, it has been reported that different architectures and hyperparameters can impact the performance of DCNNs as well. Typically, supervised approaches are superior (compared to unsupervised and self-supervised approaches) [14–16]. That is because the optimization of the parameters within the DCNN mathematical model (architecture), is achieved based on the calculated error between the DCNN's current output and the required ground truth output (i.e., input: corrupted image → DCNN → current output image -vs- ground truth: the respective equivalent to the input artifact-free image). However, real XCT training datasets (corrupted) and their respective equivalent artifact-free data are hard to obtain. In unsupervised learning, input images are dissimilar to the ground truth images, therefore overall performance is decreased [14,15]. Moreover, in current studies, each artifact type has been tackled separately (i.e., noise, or blur, or ring artifacts).

In this work, we present a multilevel and multiscale deep learning framework (BAM SynthCOND) employing novel DCNNs, trained in a supervised manner on low resemblance (if compared to experimental) synthetic materials XCT data, for treating noise and blur in experimental XCT reconstructions. We also show that by denoising the XCT data we also reduce ring artifacts. We applied our conditioning methods directly to the reconstructions and not to individual projections for the sake of generality. In the first case, the number of samples (i.e., the numerous projections) is large and, therefore, any remaining artifacts after conditioning, can easily be smeared out by a sophisticated iterative reconstruction algorithm. To our knowledge, there is virtually no public literature on materials XCT data conditioning with deep learning techniques, in which synthetic XCT training data are employed as the ground truth. Novel DCNNs architectures are introduced. Appropriate training and forwarding strategies are proposed for a successful training generalization when synthetic XCT data are employed. It is shown that this leads to successful conditioning of experimental XCT data. The term forwarding strategy refers to: the slicing method of the testing data (to be conditioned) into smaller batches, the subsequent passage of these batches through the working DCNNs, and their recombination into the final conditioned XCT data volumes. In the case of a multi-view approach/slicing, the recombination into a single final volume is performed with an appropriate fitting function that combines the conditioned views. An example of the forwarding strategy pipeline is the

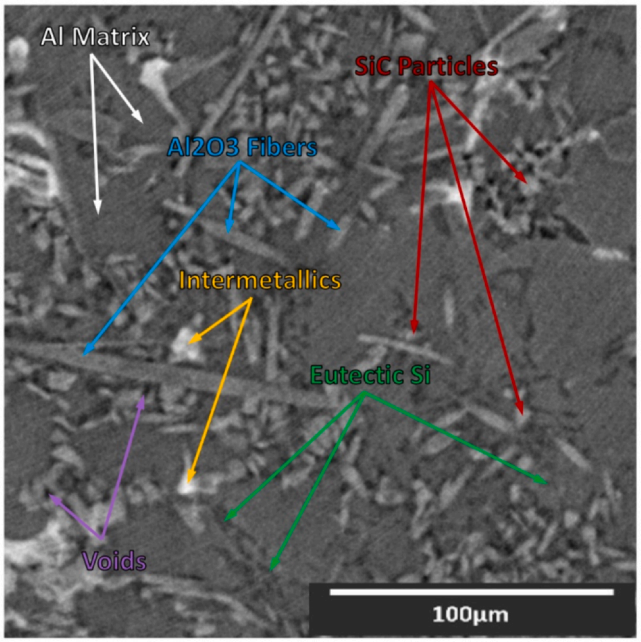

Fig. 2. XCT reconstruction slice of the AlSi12CuMgNi MMC xy-plane view). The different phases of the microstructure (see text) are indicated.

following: rotate/permute initial volume in various angles/planes creating multiple new volumes (views), slice these volumes into batches, condition the batches, combine the conditioned batches according to their reference volume, rotate/permute each conditioned volume back to initial position, combine the resulting conditioned volumes into single volume with a fitting function.

1.2. Research approach outline

The research steps undertaken are outlined below and graphically in Fig. 1:

As experimental artifact-free XCT training data are very hard to obtain, synthetic XCT data were instead employed for training. These were generated to mimic XCT reconstructions, both in terms of structural resemblance and grayscales. Two synthetic training/validation/testing dataset groups were produced for the denoising and deblurring cases, respectively.

2D and 3D multiscale, multilevel, in-house designed DCNN architectures were developed to denoise and deblur XCT reconstructions. These were trained and validated with the synthetic XCT training/validation datasets. Different DCNN architectures were utilized for each task.

The best performing input dimension (2D or 3D) for the built DCNNs and the most suitable forwarding strategies were identified for each case individually (denoising, deblurring), based on the conditioning performance on artificially corrupted synthetic XCT data (i.e., the synthetic testing datasets). For the multi-view case, the fitting functions investigated were the mean or median functions.

Based on the above selection, it was assessed whether the selected denoising/deblurring DCNNs could consistently perform irrespective of the initial noise and blur levels. This task was performed by assessing the conditioning performance on progressively increasing corrupted synthetic XCT data (new synthetic testing dataset, noise and blur combined).

As a last conditioning step (final pass), it was examined whether a low-intensity Non-Local Means (NLM) filter [7,8] could further improve the overall performance, formulating the following sequential conditioning framework: {Deep Denoising + Deep Deblurring + NLM filter}.

Lastly, the established conditioning framework (i.e., best performing input dimension and forwarding strategy for denoising and deblurring, respectively) was tested against experimental XCT (testing) datasets to determine whether the performance was comparable to the conditioning performance based on synthetic XCT testing datasets.

2. Material description

We used available XCT datasets of AlSi12CuMgNi metal matrix composites (MMC) reinforced with: {0%vol Al_2O_3 short fibers, 15%vol SiC particles} and {7%vol Al_2O_3 short fibers, 5%vol SiC particles}. Cast near eutectic Al-Si alloys are the typical materials utilized by the automotive industry for engine pistons [17–19]. Presently, interest grows in the aerospace industry concerning their suitability as a potential substitute to the broadly used unreinforced Al and Ti alloys [19,20], with possible applications such as: frames, aerials, and joining elements. The addition of the Si phase brings high fluidity to the melt, while transition elements such as Cu and Ni, encourage the formation of dense and steady aluminium intermetallics (IMs). The latter and the eutectic Si phase establish a 3D interconnected network within the alloy's microstructure [19,21]. Some mechanical properties (e.g., strength) are enhanced by adding ceramic particles and/or short ceramic fibers as reinforcements [17–21]. The microstructure of our MMC consists of five phases: (Al matrix, eutectic Si, IMs, short ceramic fibers, and ceramic particles), or six phases if voids and cracks are included. The material was produced by squeeze casting. The hybrid preform, where the molten alloy was infiltrated, had a mat of planar-randomly oriented (xy-plane) reinforcing fibers and the reinforcing particles randomly distributed. The detailed experimental procedure and equipment used for the Synchrotron XCT imaging are described in [19]. Various measurements were made to have datasets with various artifact intensities. In Fig. 2, a 512 × 512-pixel cross-section of a high-quality XCT reconstruction of the material is displayed. We notice that some phases possess comparable X-ray attenuation coefficients (particles, fibers, Al matrix, and some intermetallics).

3. Method development

3.1. Synthetic Al-Si MMC microstructure generation

In order to generate suitable training data for the deep neural networks, the in-house synthetic XCT MATLAB library (BAM SynthMAT) by Tsamos et al. [17] was employed. The microstructures were generated to mimic XCT data in terms of structural resemblance and simulated grayscales. The synthesis process is presented in detail in [17]. As we use the same material, identical statistics were adopted from [17] to synthesize eight 512 × 512 × 512 (voxel) Al-Si MMC microstructures. Out of these, seven were randomly selected to generate the training/validation data, while the last one was reserved for testing (synthetic testing data).

3.2. Augmentations on all training and validation synthetic XCT datasets (Denoising and Deblurring cases)

In [17], it is suggested that ± 10% brightness and contrast augmentations should be used on the synthetic training/validation data. The reason is that the experimental grayscale distributions cannot be precisely replicated, irrespective of the care taken to synthesize artificial XCT data for training. Since synthetic data incorporate only a few grayscales to represent the various microstructural phases, it was proven that the augmentations mentioned above could ensure good generalization with knowledge gained from synthetic data and, therefore, satisfactory performance of the DCNN on experimental datasets. In this work, we increased the intensity of these augmentations to ± 20% as we found this more suitable for conditioning problems.

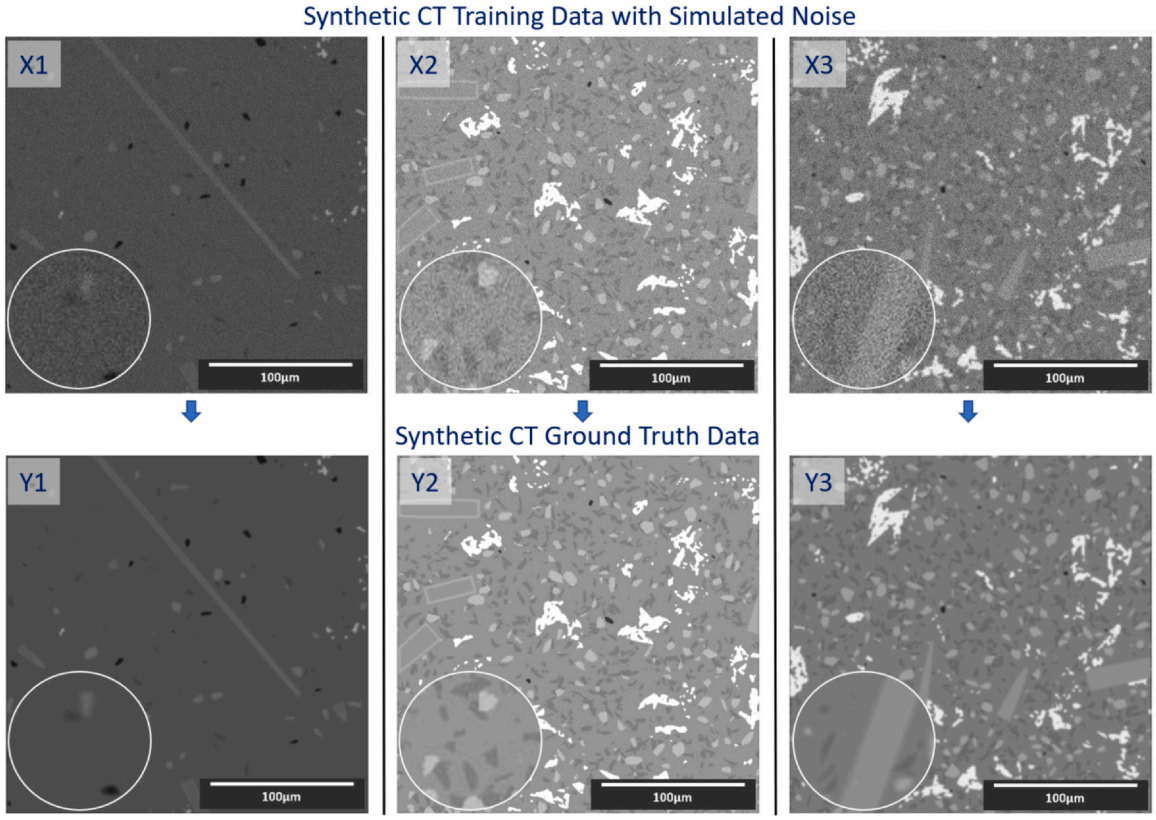

Fig. 3. 2D Denoising training/validation sub-images generated from the synthetic XCT data. X: Input images with added Gaussian noise (1: brightness, 2: contrast, 3: blurring, 4: noise augmentations). Y: Ground Truth images without noise (1: brightness, 2: contrast, 3: blurring augmentations).

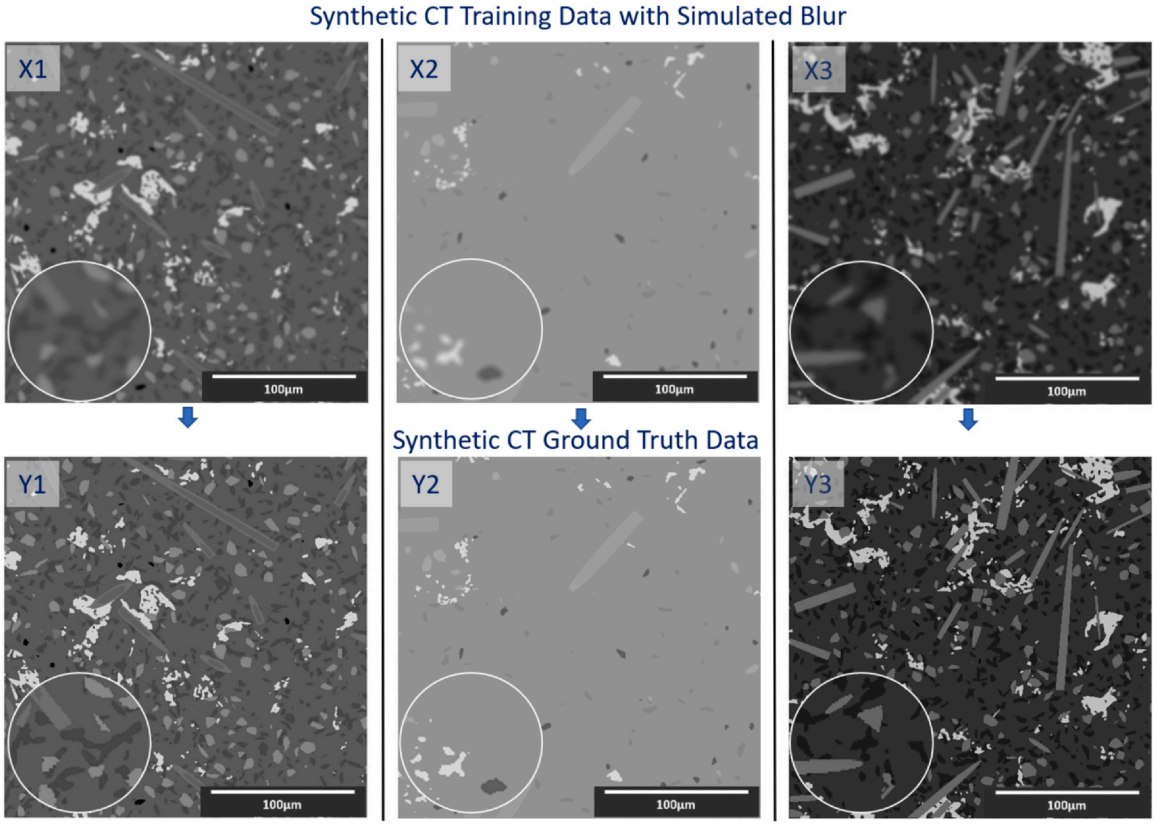

Fig. 4. 2D Deblurring (Sharpening) training/validation sub-images generated from the synthetic CT data. X: Input images with added Gaussian blur or average blur (1: brightness, 2: contrast, 3: blur augmentations). Y: Ground Truth images without blur (1: brightness, 2: contrast augmentations).

Table 1
Training and Validation Data Summary.

	Total Sub-Image/Sub-Volume pairs	Training pairs	Validation pairs
2D Denoising	3584	3136	448
3D Denoising	5103	4465	638
2D Deblurring	3584	3136	448
3D Deblurring	5103	4465	638
	Augmentations on pairs		
	Contrast & Brightness	**Gaussian Noise**	**Gaussian/Average Blur**
2D/3D Denoising - Input	YES	YES	YES
2D/3D Denoising - Ground Truth	YES	NO	YES
2D/3D Deblurring - Input	YES	NO	YES
2D/3D Deblurring - Ground Truth	YES	NO	NO

3.3. Training and validation synthetic XCT datasets for rectifying noise

The synthetic data were initially artifact-free, but certain synthetic artifacts were introduced depending on the target network (denoising or deblurring DCNN). For the denoising case, the ground truth image of experimental XCT data is not always sharp. Therefore, in addition to the above augmentations (described above in 3.2), two random blurring types and intensities were introduced on both the training and validation data. Gaussian or average blur was applied with a randomly varying filter radius (sigma = 0–5). This helped training a denoising neural network to eliminate noise in both blurry and sharp images. The resulting images were chosen as the ground truth. Finally, Gaussian noise with randomly varying standard deviation $(0-20)$ was applied (8-bit image range: 0–255) to the ground truth images. The negative values emerging after the application of the noise window were nulled. The added noise type and the brightness augmentations effectively simulated Poisson noise, the dominant noise present in Low Dose XCT (LDXCT). The resulting noisy data were used as input to the 2D and 3D denoising nets. Examples are displayed in Fig. 3.

3.4. Training and validation synthetic XCT datasets for rectifying blur

For the deblurring case, no noise was added to the synthetic data, as it was assumed that blurry input data were thoroughly denoised or noise-free. Therefore, only brightness and contrast augmentations were adopted. The input data were generated by applying Gaussian or average blur with randomly varying intensities, precisely as in the case of the denoising training data. Examples are illustrated in Fig. 4.

3.5. 2D and 3D training and validation data slicing

2D and 3D training/validation datasets were generated from the seven synthetic volumes. The input size for the 2D network(s) was set as 512×512 pixels (sub-image). The slicing was performed along the plane of the fibers (xy in Fig. 3 and Fig. 4), resulting in $7 \times 512 = 3584$ (512×512 pixels) 2D images. From these, 3136 (87.5%) were randomly selected as training data and 448 (12.5%) as validation data. The input size for the 3D network(s) was set as $64 \times 64 \times 64$ voxels (sub-volumes). The slicing was performed with a stride = 56, consistent in all x, y, z directions, resulting in $7 \times 9^3 = 5103$ ($64 \times 64 \times 64$) 3D images. From these, 4465 images (87.5%) were randomly selected as training data, and the remaining 638 images (12.5%) as validation data. Lastly, the previously discussed augmentations and problem-specific noise and/or blur were introduced accordingly during the slicing to each sub-volume and sub-image in a random fashion (i.e., slicing 1st, brightness/contrast augmentations 2nd, problem-specific noise and/or blur augmentations 3rd). This effectively doubled the number of sub-volumes and sub-images into pairs (X: inputs, Y: ground truths). The whole process is summarized in Table 1.

3.6. Denoising and deblurring convolutional neural networks

3.6.1. Proposed architectures introduction

Two different in-house architectures were designed, incorporating the latest advancements in image analysis with Deep Learning. One was

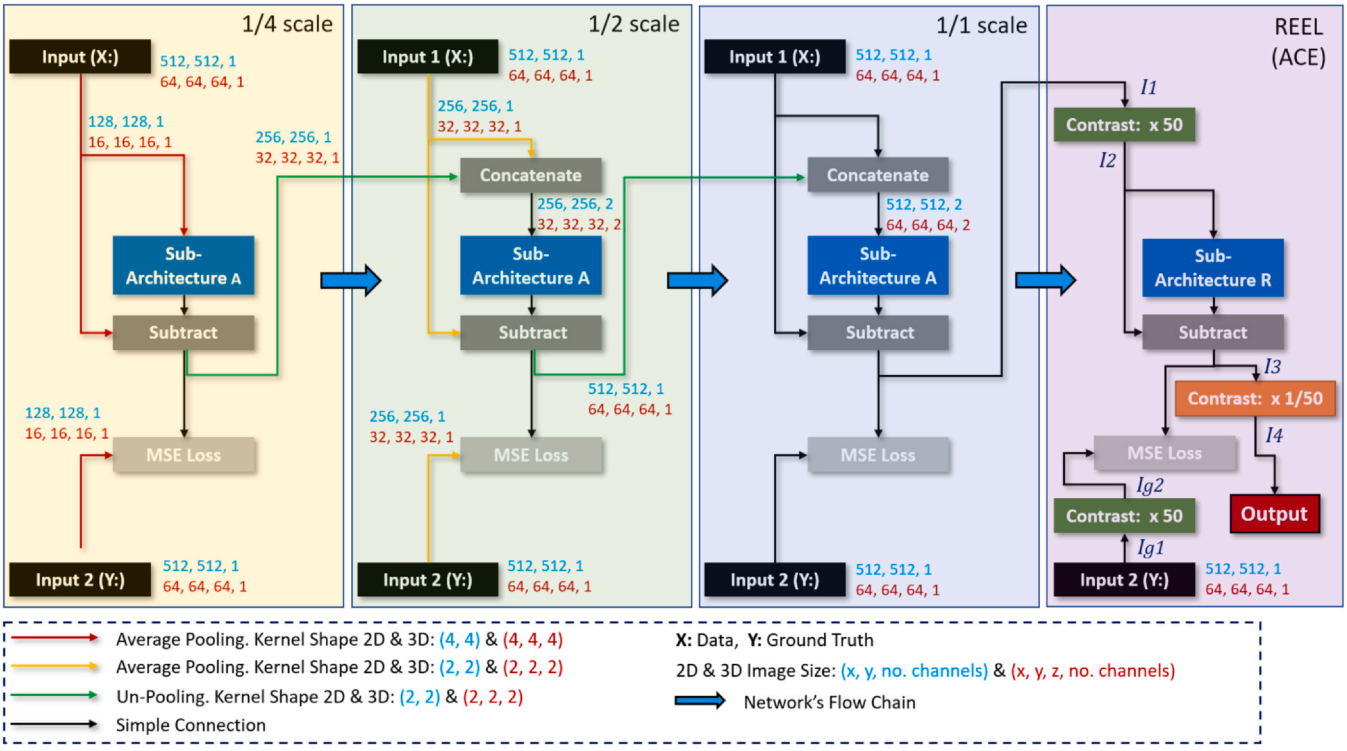

Fig. 5. < 2D/3D ACEnet_Denoise > Multiscale Global Architecture, including the proposed final REEL. Input 2D: (512, 512, 1). Input 3D: (64, 64, 64, 1).

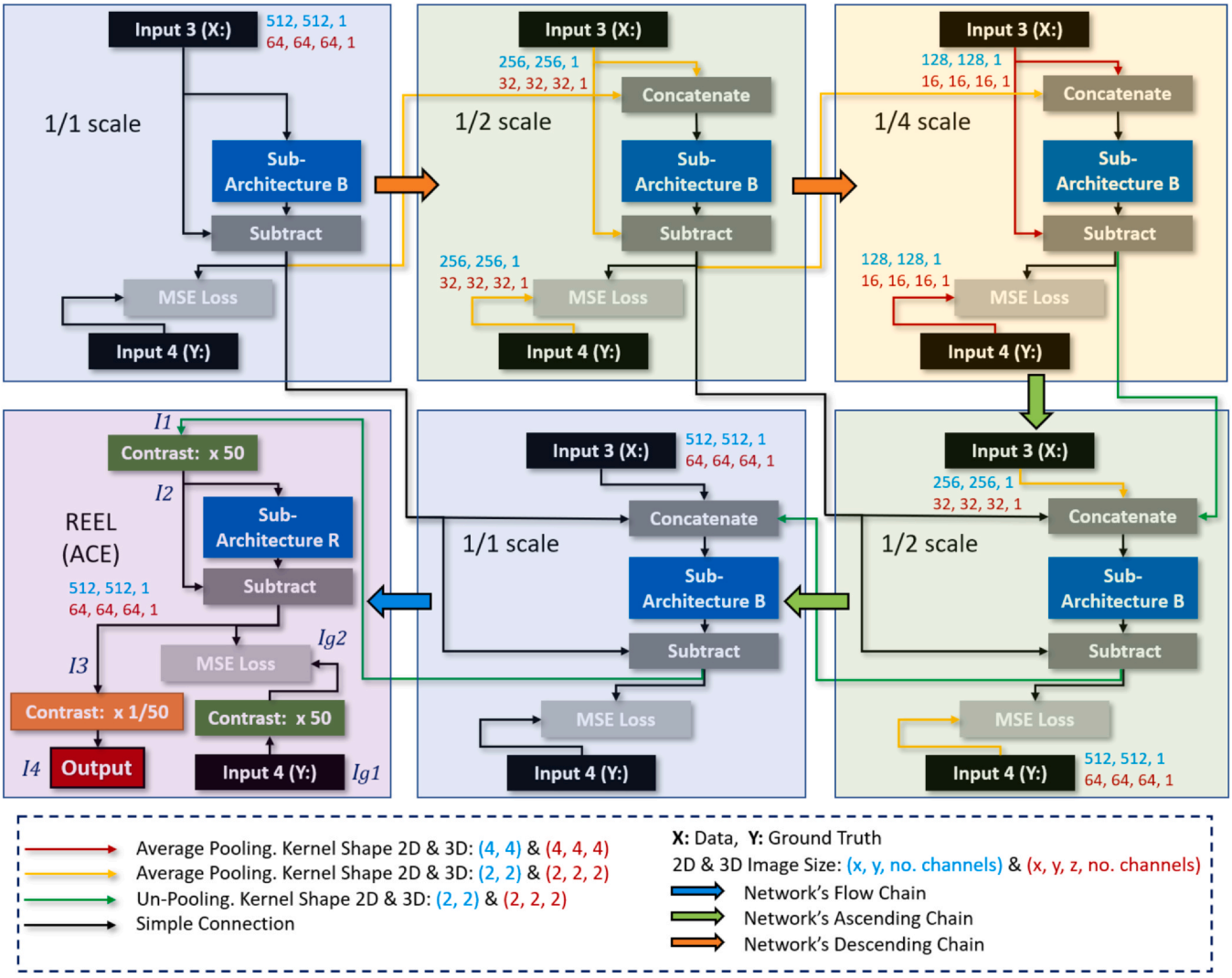

Fig. 6. < 2D/3D ACEnet_Deblur > Multiscale Global Architecture, including the proposed final REEL. Input 2D: (512, 512, 1). Input 3D: (64, 64, 64, 1).

responsible for rectifying noise and one for sharpening blur. Both architectures were implemented into 2D and 3D versions. Thus, in total, four deep convolutional neural networks were built. All architectures incorporated multiple scales, each responsible for tackling the problem independently at different image scales (1/4, 1/2, 1/1). However, the scales were arranged in a different order in the two architectures. Moreover, a proposed final same-scale (1/1) Remaining Error Enhancing Level (REEL) employing the novel Assertive Contrast Enhancement (ACE) training strategy, was implemented in both architectures. This level was responsible for providing a further rectifying pass to the final output. All scales/levels were trained sequentially with individual Mean Squared Error Loss (MSE) functions. Where applicable, the output of a previously trained scale(s) was(were) upscaled (or downscaled) and concatenated with the input of the next scale/level. This was inspired by Karras et al. multiscale approach in StyleGAN net [22]. Finally, all architectures allowed residual/skip connections, subtracting each scale/level input from the output. This effectively forced the networks to identify and subtract the noise or blur from the corrupted image instead of extracting the ground truth image from the corrupted one. This approach has previously been proven to produce better results and faster convergence than non-residual nets [23]. Although the literature offers a vast number of good architectures for data conditioning, to the best of our knowledge there are no architectures combining all the features we needed to tackle our problem (i.e., multiscale training, residual connections, dilated convolutions, advanced activation functions). In addition to combining such features, we propose novel ACE blocks. Thus, we introduce a completely new type of deep neural nets: i.e., the ACEnets.

3.6.2. The 2D/3D denoising network main architecture (2D/3D ACEnet_Denoise)

The 2D/3D Denoising network(s) consists of 3 different scales, sequentially linked in ascending order, and the proposed REEL linked at the end: (1/4 → 1/2 → 1/1 → REEL). The transition between the scales is achieved with Average Pooling and Unpooling (Upsampling) layers. Skip connections are established between every scale/level input and output. The design is modular as each scale sub-architecture (Sub-Architecture A) is identical across all scales. However, the REEL carries its distinct sub-architecture (Sub-Architecture R). The global multiscale architecture of the proposed 2D/3D Denoising networks(s) is graphically illustrated in Fig. 5.

3.6.3. The 2D/3D deblurring network main architecture (2D/3D ACEnet_Deblur)

Similarly, the 2D/3D Deblurring network(s) consists of 3 different scales. However, unlike the Denoising network, these are sequentially linked in descending-ascending order: (1/1 → 1/2 → 1/4 → 1/2 → 1/1 → REEL), intuitively resembling a UNet architecture [24]. The transition between the scales is performed again with Average Pooling and Unpooling layers. In addition, the 1/2 and 1/1 scales in the ascending

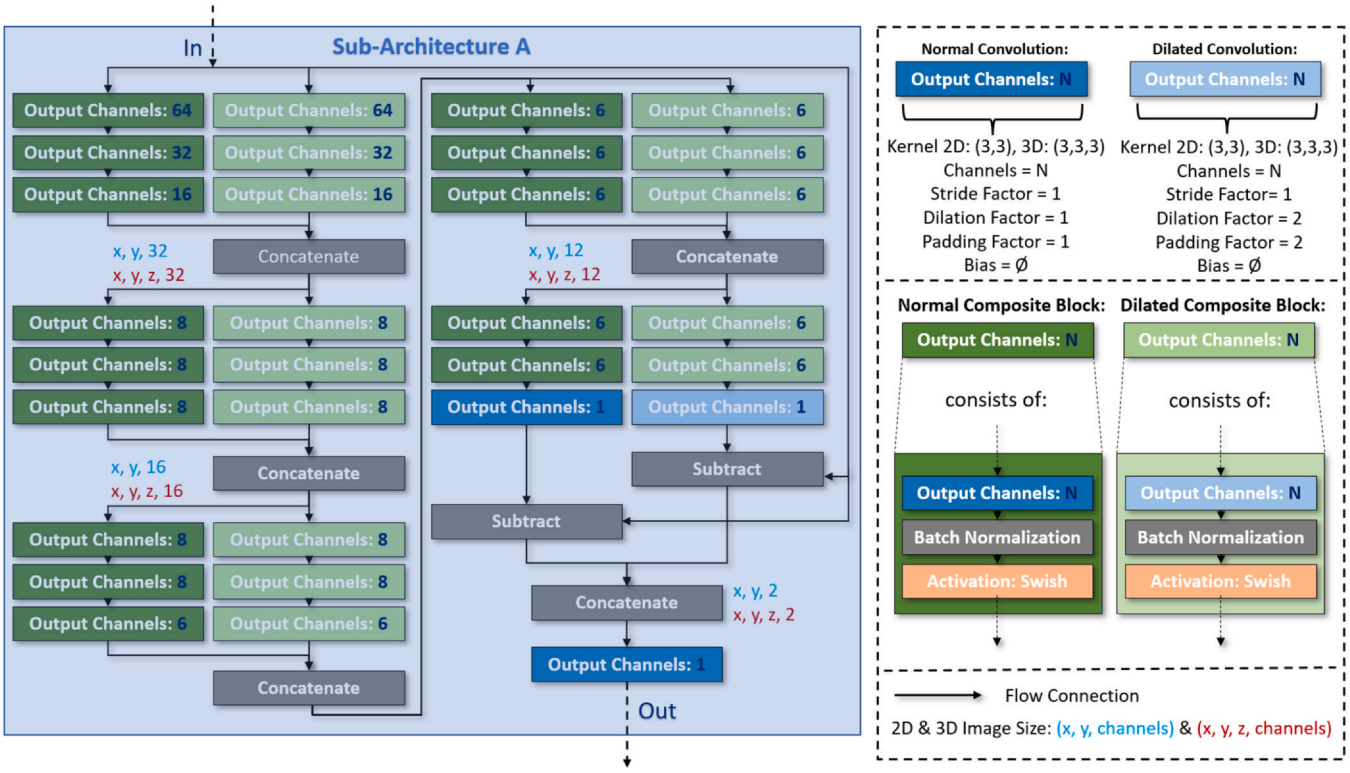

Fig. 7. The Sub-Architecture A (present within the 2D/3D Denoising networks).

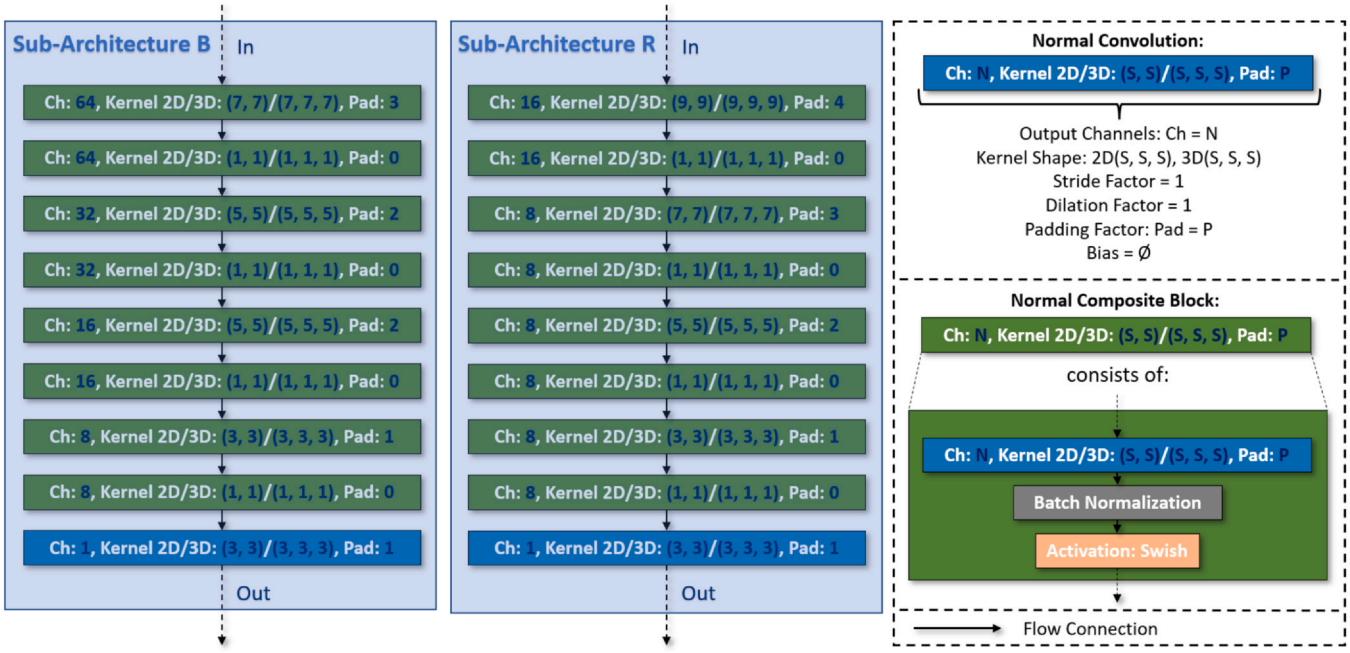

Fig. 8. The Sub-Architecture B and Sub-Architecture R (present within the 2D/3D Deblurring networks and present within all networks respectively).

chain receive input via concatenation both from the previous scale (in the sequential order) and their descending chain equivalents (1/2 and 1/1) scale outputs. Furthermore, the residual feedback in these two scales is received from their descending chain equivalents (1/2 and 1/1) scale outputs, and not from their inputs. All other scales have the regular residual skip connections previously discussed. The sub-architecture (Sub-Architecture B) of each scale is the same across all scales as before. The global multiscale architecture of the proposed 2D/3D Deblurring networks(s) is illustrated graphically in Fig. 6.

3.6.4. The remaining error enhancing level (REEL) - assertive contrast enhancement (ACE)

In any mathematical optimization problem, further improvement becomes progressively challenging as the error gets smaller. Convolutional neural networks average the training error across the whole image to update their parameters during backpropagation (training). This average operation is a desirable generalization effect. From our experience, this can result in an excellent performance in the bulk, single gray-level regions, of an image, and a slightly inferior

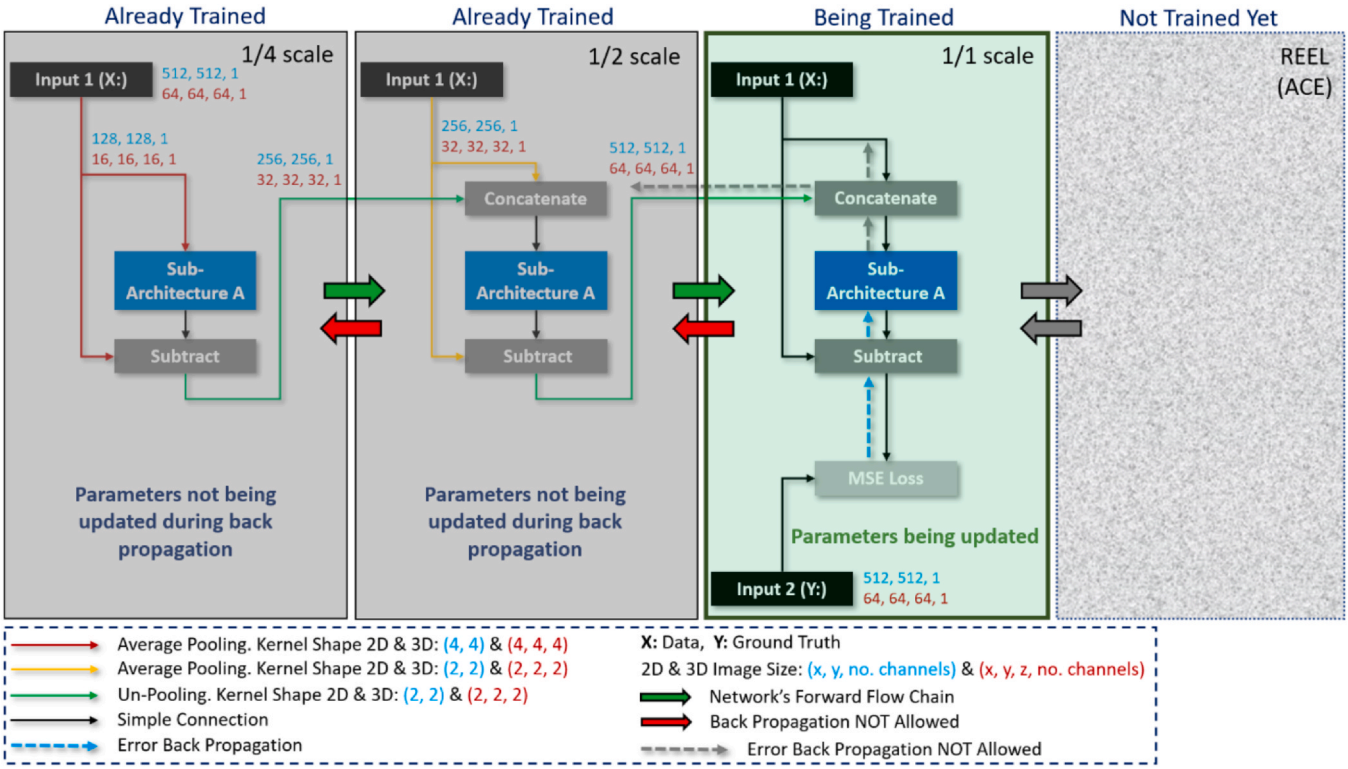

Fig. 9. Back propagation of the error (parameters update) during the (1/1) scale training in the 2D/3D Denoising Nets.

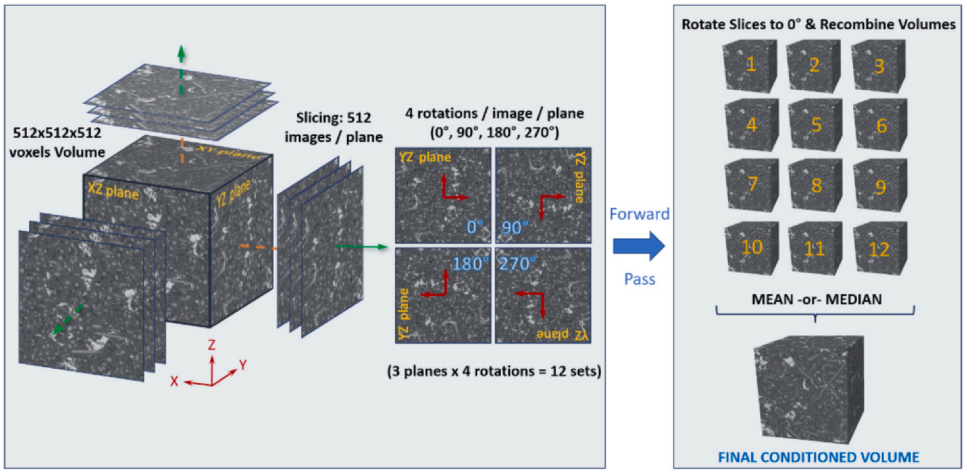

Fig. 10. The 2D_MultiView_(Mean or Median) Forwarding Strategy Workflow. Note that for 2D_SingleView the strategy is similar but contains only the xy plane and the 0° rotation.

performance at the interfaces. The reason is that bulk regions are usually dominant in an image. Therefore, their contribution to the overall error minimization is significantly amplified compared to the interface regions. As the name suggests, the proposed REEL tackles this issue by amplifying the remaining errors by means of Assertive Contrast Enhancement training (ACE). This takes place on the output of the last (1/1) scale in all nets and on the ground truth image. More specifically, the last scale output (I_1) and ground truth (I_{g1}) images contrasts are increased by a factor of 50, Equations: (1) and (2), respectively, before being fed as (I_2) and (I_{g2}) into the REEL's sub-architecture and loss function, respectively.

$$I_2 = (I_1 - \bar{I}_1) \times 50 + \bar{I}_1 \quad (1)$$

$$I_{g2} = (I_{g1} - \bar{I}_1) \times 50 + \bar{I}_1 \quad (2)$$

$$I_4 = (I_3 - \bar{I}_1)/50 + \bar{I}_1 \quad (3)$$

We found that this approach (ACE training) further increases the final image quality without effectively increasing the computational effort. Finally, during the forward pass, the REEL's output image (I_3) contrast is reduced by a factor of 50 (I_4) back to the initial level, (Eq. (3)). The contrast center ($\bar{I}_1$) required for the calculations is evaluated from the average pixel/voxel intensity from across the whole image (I_1) for all cases. The REEL's main building blocks are illustrated in Fig. 5 and Fig. 6.

3.6.5. The denoising network sub-architecture A

Sub-Architecture A consists of parallel stacks of normal and dilated convolutions, with the output of the convolutional stacks being concatenated every three blocks. Moreover, two residual skip connections are established at the end of the parallel stacks (which are

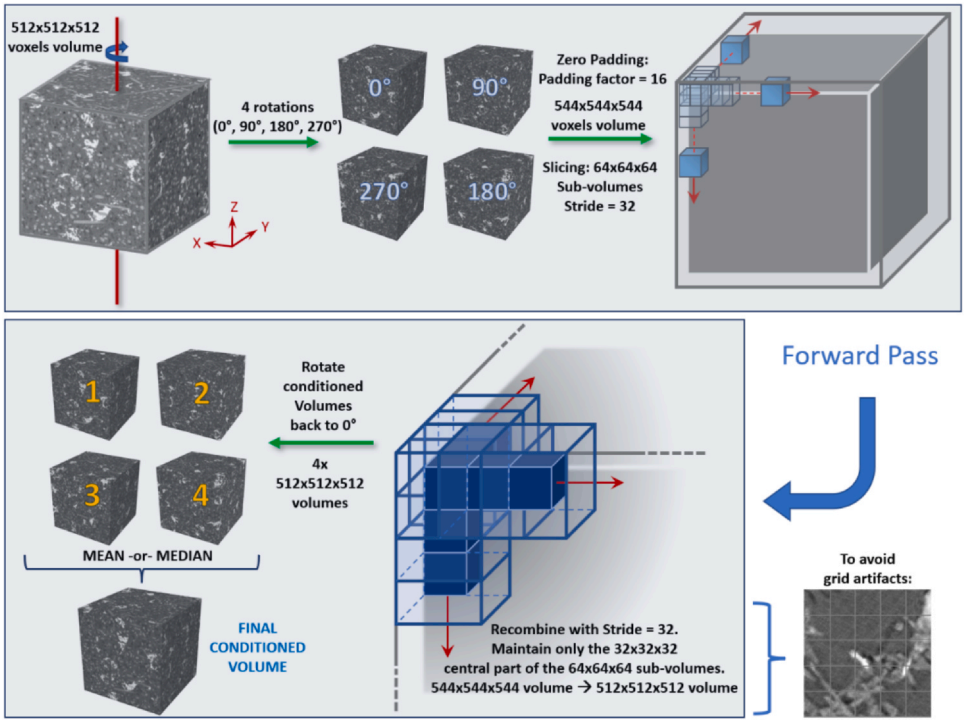

Fig. 11. The 3D_MultiView (Mean or Median) Forwarding Strategy Workflow. Note that for 3D_SingleView the strategy is similar but contains only the 0° rotation (and no fitting function).

Table 2
Selection of best Denoising/Deblurring Neural Network and Forwarding Strategy combination (Green: Best metric value, Red: Worst metric value).

	Denoising					
	2D_SingleView	2D_MultiView_Mean	2D_Multiview_Median	3D_SingleView	3D_MultiView_Mean	3D_Multiview_Median
SSIM	0.85	0.99	0.99	0.96	0.97	0.97
HE	4.54	4.11	3.81	4.48	4.39	4.38
	Deblurring					
	2D_SingleView	2D_MultiView_Mean	2D_Multiview_Median	3D_SingleView	3D_MultiView_Mean	3D_Multiview_Median
SSIM	0.90	0.95	0.95	0.93	0.94	0.94
HE	4.28	4.29	3.95	4.68	4.58	4.55

Table 3
Combined Denoising and Deblurring performance assessment of purposedly corrupted Synthetic XCT volume with increasing 3D Gaussian Blur and Gaussian Noise. SSIM metric: Conditioned Output -vs- Artifact-Free Synthetic XCT Volume.

SSIM%			
SA	SB	SC	SD
92.4	91.5	91.7	91.7

supplementary to the residual connection in the global architecture). The padding is adjusted accordingly to maintain the same image size after every convolution (same border mode). The normal and dilated convolutions are performed with a kernel shape 2D:(3, 3) and 3D:(3, 3, 3). The dilation (where applicable) and stride factors are set as 2 and 1, respectively, for all directions. Every convolution block is followed by a batch normalization block and an activation function (forming composite blocks), apart from the convolutions before the residual blocks. The batch normalization block decay rate and epsilon parameters are set as 9e-1 and 1e-4, respectively. The adopted activation function is Swish [25] for its continuity and superiority compared to the ReLU function. The Sub-architecture A and the implemented output channels for each convolution are shown graphically in Fig. 7.

3.6.6. *The deblurring network sub-architecture B*

The Deblurring networks' Sub-Architecture B consists of only sequentially stacked normal composite blocks (normal composite block: normal convolution, batch normalization, and activation function). The kernel shapes vary from 2D:(1, 1) and 3D:(1, 1, 1) to 2D:(7, 7) and 3D:(7, 7, 7). As before, the padding is adjusted accordingly to maintain the same image size after every convolution. The batch normalization parameters and employed activation function are the same as Sub-Architecture A. The exact Sub-Architecture B and the implemented output channels for each convolution are shown in Fig. 8.

3.6.7. *The REEL sub-architecture R*

The REEL's Sub-Architecture R is comparable to Sub-Architecture B. However, the employed convolutional kernel shapes vary from 2D:(1, 1) and 3D:(1, 1, 1) to 2D:(9, 9) and 3D:(9, 9, 9). The exact Sub-Architecture R and the implemented output channels for each convolution are shown in Fig. 8.

3.6.8. *Training strategy and parameters*

As previously discussed, all network individual scales/levels were trained sequentially (one at a time) with independent MSE Loss functions. When applicable, they received further input from the previous (already trained) scale. Moreover, only the scale/level parameters being trained were updated during backpropagation. This strategy is illustrated in Fig. 9, where the (1/1) scale of the 2D/3D Denoising

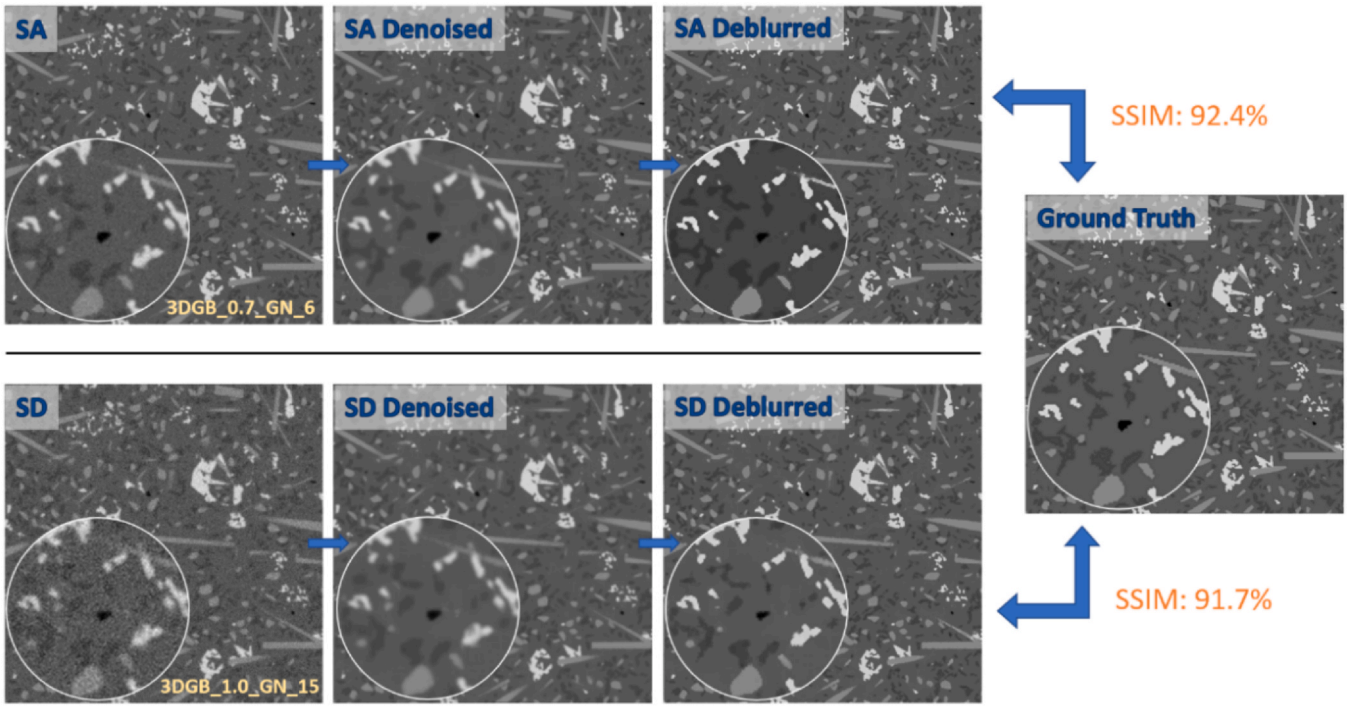

Fig. 12. Conditioning results for the least (SA) and most (SD) corrupted synthetic XCT volumes. Sequential application of 2D denoising and 2D deblurring networks with the 2D_MultiView_Median forwarding strategy.

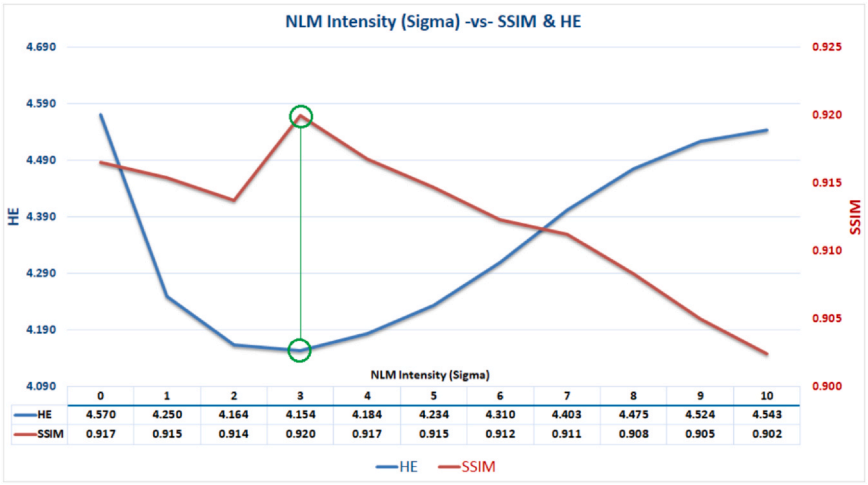

Fig. 13. Application of a NLM filter with varying intensity: sigma = 1–10, and constant smoothing factor = 1. SSIM and HE values on the conditioned (denoised and deblurred) Synthetic XCT: SD Dataset.

Networks is virtually exemplarily trained. All networks were designed and trained with Sony's Neural Network libraries [26] on a workstation equipped with a GeForce RTX 3090, a Pentium i7 CPU, and 32 GB of memory. The ADAM algorithm [27] was chosen as the optimizer (parameters: Initial Learning Rate/Alpha = 1e-4, Beta1 = 0.9, Beta2 = 0.999, updated every iteration), and the selected input batch size was 8. The Learning Rate (LR) was updated exponentially at every epoch with a Learning Rate Multiplier: LRM = 0.92 (i.e., LR = LR_0 × (0.92^{epoch})). Furthermore, a random shuffling strategy was adopted for the training datasets on each epoch. Finally, the maximum number of epochs was set as 100. Both training and validation errors were recorded, but the final learnable parameters were taken from the epoch that minimized the validation error.

4. Testing on purposedly corrupted synthetic XCT data: results and discussion

4.1. Generality on the quality metrics

In this section, the designed networks are firstly tested as stand-alone applications and subsequently combined in a sequential framework (Denoising + Deblurring). The reserved eighth synthetic XCT volume is employed for the task. The metrics used for the assessment are the Structural Similarity Index Measure (SSIM) [28], the Histogram Entropy (HE) [29,30], and the quantitative (0 − 1) Blur Metric (BM) by Crété-Roffet et al. [31]. SSIM is a well-established [34–36] full-reference metric for which the output quality of the conditioned data is

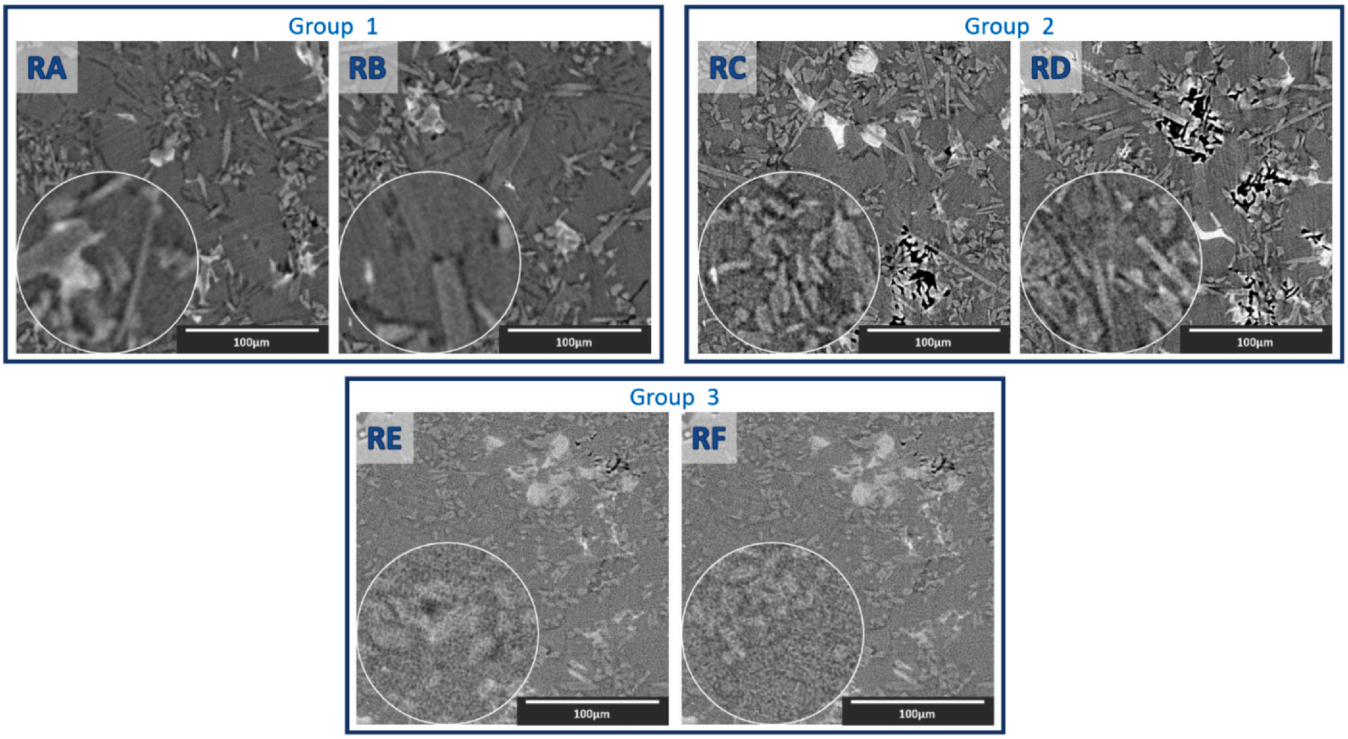

Fig. 14. Slices of experimental XCT reconstruction groups before conditioning. (See text for details).

based on the similarity with the corresponding artifact-free ground truth (0–1: 1 indicate 100% similarity). The similarity assessment is based on luminance, contrast, and structure altogether. Therefore, the metric is superior to other common metrics such as: Mean Squared Error (MSE) or Peak Signal to Noise Ratio (PSNR) [32–34], which evaluate image quality based on absolute errors. Thus, we consider SSIM as an excellent conditioning performance assessment tool for purposedly corrupted synthetic XCT data. However, in the case of the experimental XCT datasets, there are no available ground truth volumes for comparison; hence, SSIM is not relevant. On the other hand, HE is a no-reference image entropy/quality metric requiring no ground truth data [12,13]. HE measures statistical randomness to characterize the texture of the image [29] calculated by:

$$HE = -\sum_{k} p_k \quad \log_2(p_k) \tag{4}$$

Where k is the number of gray levels (256 for 8-bit images) and p_k is the probability of gray level k. According to [30], HE is defined as the entropy of a histogram bucket of an image. This can be interpreted as the entropy of the probability distribution of the values within that bucket. (The probability of each value is given by the frequency divided by the total number of attribute values). HE is highly affected by the number of existing gray levels in an image. Blur and noise can increase the number of gray levels present, increasing the HE value [12]. Generally, the lower the HE, the higher the quality of an image. However, data with many structural gray levels present can still bear a high HE irrespective of any existing artifact (this is the case of XCT data of materials with many microstructural constituents of different densities). Any conditioning can only marginally improve HE in such cases. Lastly, a possibility exists where successful sharpening could reveal hidden noise or hidden structural gray levels that were perhaps smeared out before conditioning because of blurring. This could cause an increase in HE instead.

4.2. Individual network performance testing

We also test which respective 2D or 3D trained version of the neural networks performs better. For the 2D/3D Denoising and 2D/3D Deblurring networks, this is achieved by purposedly corrupting and then conditioning the eighth synthetic XCT volume with Gaussian noise of standard deviation = 20 (8-bit image: 0 – 255 bits gray level range) or with 3D Gaussian blur with sigma = 1, respectively. Furthermore, various forwarding strategies are tested to identify the one(s) maximizing conditioning performance. For both 2D networks, a simple forwarding strategy is to slice the corrupted volume into 512 images (size: 512 × 512) moving perpendicularly to the xy (top) plane, perform the forward pass through the neural networks, and finally recombine the images into the conditioned volume (2D_SingleView). A more sophisticated method is to slice the corrupted volume along all three xy, yz, and xz planes and further rotate each image four times with an angular increment of 90° (i.e., at 0°, 90°, 180°, 270°). Thus, twelve similar conditioned volumes are produced after the forward pass and recombination. The final conditioned volume can be determined by evaluating the Mean or Median volume of the latter (2D_MultiView_Mean and 2D_MultiView_Median, respectively). The workflow of this forwarding strategy is illustrated in Fig. 10. For both 3D networks, the volume is initially zero-padded with padding size = 16. Then, the volume is sliced into 64 × 64 × 64 sub-volumes (the input size of the 3D nets), moving across all directions with a stride = 32. Finally, after the forward pass, only the 32 × 32 × 32 central region of each conditioned sub-volume is conserved for the recombination (3D_SingleView). This method ensures 3D recombination continuity, avoiding the otherwise resulting grid-shaped artifacts at the sub-volume connection regions (grid artifacts arise from boundary uncertainties). Moreover, a multiple-view approach is also tested for the 3D case by applying four rotations (0°, 90°, 180°, 270°) to the whole volume (rotation axis: z) prior to slicing. Therefore, after the forward pass, four similar conditioned volumes are recombined. The final conditioned volume is determined again by evaluating the Mean or Median volume of the latter (3D_MultiView_Mean and 3D_MultiView_Median, respectively). The workflow of this forwarding strategy is illustrated in Fig. 11. The metric results for the Denoising and Deblurring networks of the above analysis are given in Table 2. An omnidirectional eight voxel trim is necessary on the conditioned volume to ensure comparability. This trim eliminates any image irregularities at the external boundaries (512 × 512 × 512 volumes trimmed to 496 × 496 × 496 volumes). The best neural networks/

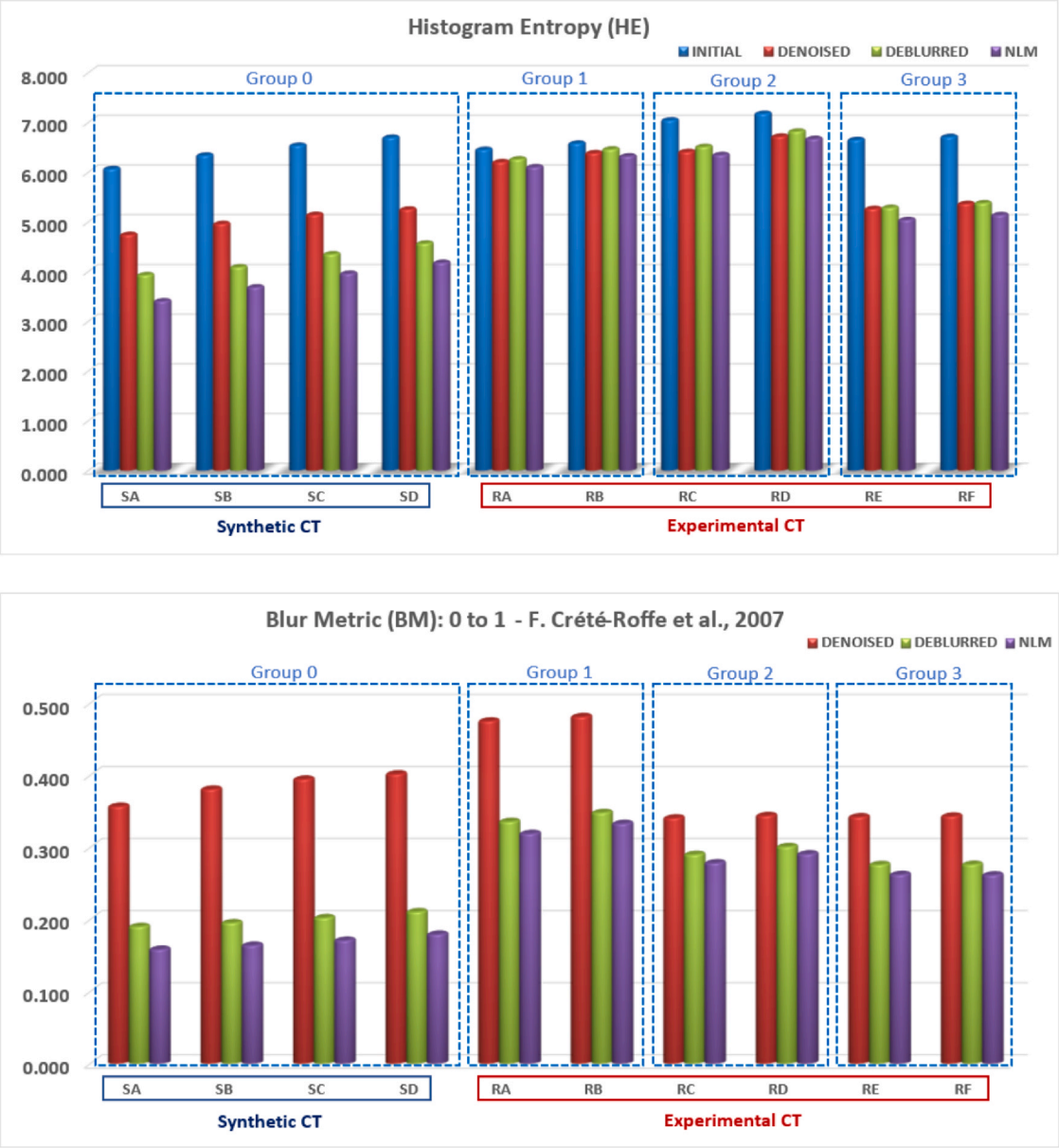

Fig. 15. Resulting HE and BM of both synthetic and experimental XCT Volumes from each step of the conditioning process.

forwarding strategies combination is the 2D Denoising and 2D Deblurring networks; both coupled with the 2D_Multiview_Median forwarding strategy. More specifically, according to the SSIM metric results, 99% and 95% structural similarity is achieved for the denoised and deblurred (purposedly corrupted with noise and blur individually) synthetic XCT volumes, respectively. HE results further support these findings. Thus, the applications and results that are presented in the following sections are solely based on these combinations.

4.3. Performance consistency results

We assess the combined Denoising and Deblurring networks sequential application for conditioning performance consistency. We again employ the eighth synthetic XCT volume and corrupt it with increasing intensities of 3D Gaussian blur and Gaussian noise combined (blur and noise are introduced one after the other). In total, we prepare four artificially corrupted synthetic XCT volumes with the following specifications:

Synthetic XCT testing datasets:
SA: Gaussian blur sigma = 0.7, Gaussian noise stand.dev. = 06.
SB: Gaussian blur sigma = 0.8, Gaussian noise stand.dev. = 09.
SC: Gaussian blur sigma = 0.9, Gaussian noise stand.dev. = 12.
SD: Gaussian blur sigma = 1.0, Gaussian noise stand.dev. = 15.

We sequentially denoise and deblur each volume, then compare the output against their artifact-free ground truth equivalent with the SSIM metric. The results of this analysis reveal that the performance is effectively consistent. An approximately constant 92% structural similarity is achieved irrespective of the initial noise and blur levels present, as it is shown in Table 3. In Fig. 12, cross-sections from the sequential conditioning progress of the least and most corrupted synthetic datasets are illustrated (SA and SD, respectively).

As the cross-sections in Fig. 12 reveal, the overall performance is very good, especially for bulk regions. The final conditioned images of the least and most corrupted synthetic CT data are almost identical. Only some structural irregularities can be seen at the edges of the smallest or thinnest objects, reasonably more evident in the most

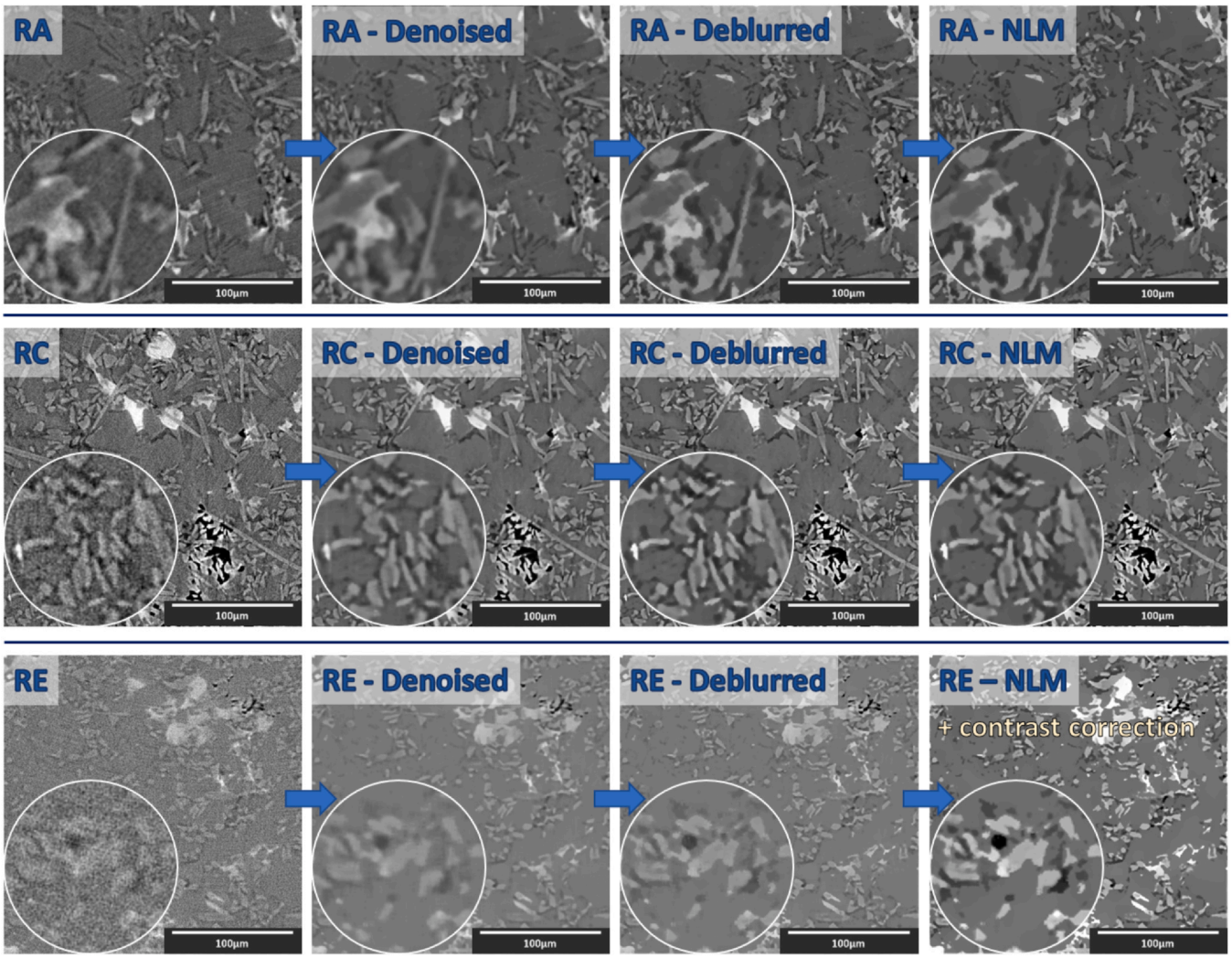

Fig. 16. Conditioning results on slices of experimental XCT volumes. Sequential application of 2D Denoising / 2D Deblurring networks with the 2D_MultiView_Median forwarding Strategy, and the final NLM filtering step.

corrupted dataset SD. However, this little amount of structural loss is generally inconsequential.

4.4. Final Pass with a low intensity NLM Filter

In the text above and in the literature, it was argued that high-intensity digital conditioning filters could result in structural image losses. Here we examine whether an NLM filter can be beneficial in further improving the conditioning result if employed after the sequential application of the denoising and deblurring networks. This is tested on the conditioned synthetic XCT dataset SD (SD Deblurred in Fig. 12) by varying the digital filter intensity: sigma = 0–10 with a constant smoothing factor = 1. As shown in Fig. 13, an NLM filter with sigma = 3 maximizes SSIM to 92% (initially: 91.7%) and minimizes HE to 4.154 (initially: 4.570). With a higher sigma we notice a drop in the SSIM value, indicative of structural losses. Thus, we propose that the process of reconstructed data conditioning can be structured as a sequential 3-level framework: {2D_Denoising with 2D_MultiView_Median strategy, 2D_Deblurring with 2D_MultiView_Median strategy, and NLM Filtering with (sigma = 3, sf = 1)} for best performance. The NLM filtering step is applied in all previously conditioned synthetic XCT datasets (SA-SD).

5. Testing/application on experimental XCT data: results and discussion

At this point we have established that the proposed Conditioning framework: {2D_Denoising with 2D_MultiView_Median strategy, 2D_Deblurring with 2D_MultiView_Median strategy, and NLM Filtering with (sigma = 3, sf = 1)}, performs well with purposedly corrupted synthetic XCT data irrespective of the initial noise and blur levels present. In this section we examine the performance of the proposed conditioning framework on experimental XCT volumes. For the task, we employ six 512 × 512 × 512 voxel experimental XCT reconstructions arranged in groups of two, with varying levels of noise and blur for each group (group 1: {RA, RB}, group 2: {RC, RD}, group 3: {RE, RF}, see Fig. 14). The experimental datasets in each group are cut from a larger dataset, hence are statistically equivalent. We apply the 3-level conditioning framework and compare the results with the synthetic XCT datasets (group 0: {SA, SB, SC, SD}) using the HE and the BM.

In Fig. 15, the resulting HE and BM values from all conditioning steps and all datasets (synthetic and experimental) are given, whereas in Fig. 16, the resulting cross-sections are illustrated for each step of the conditioning process (experimental datasets: RA, RC, and RE only). As it can be observed, HE values have a dramatic drop after each step of the conditioning process of the synthetic datasets (group: 0). These

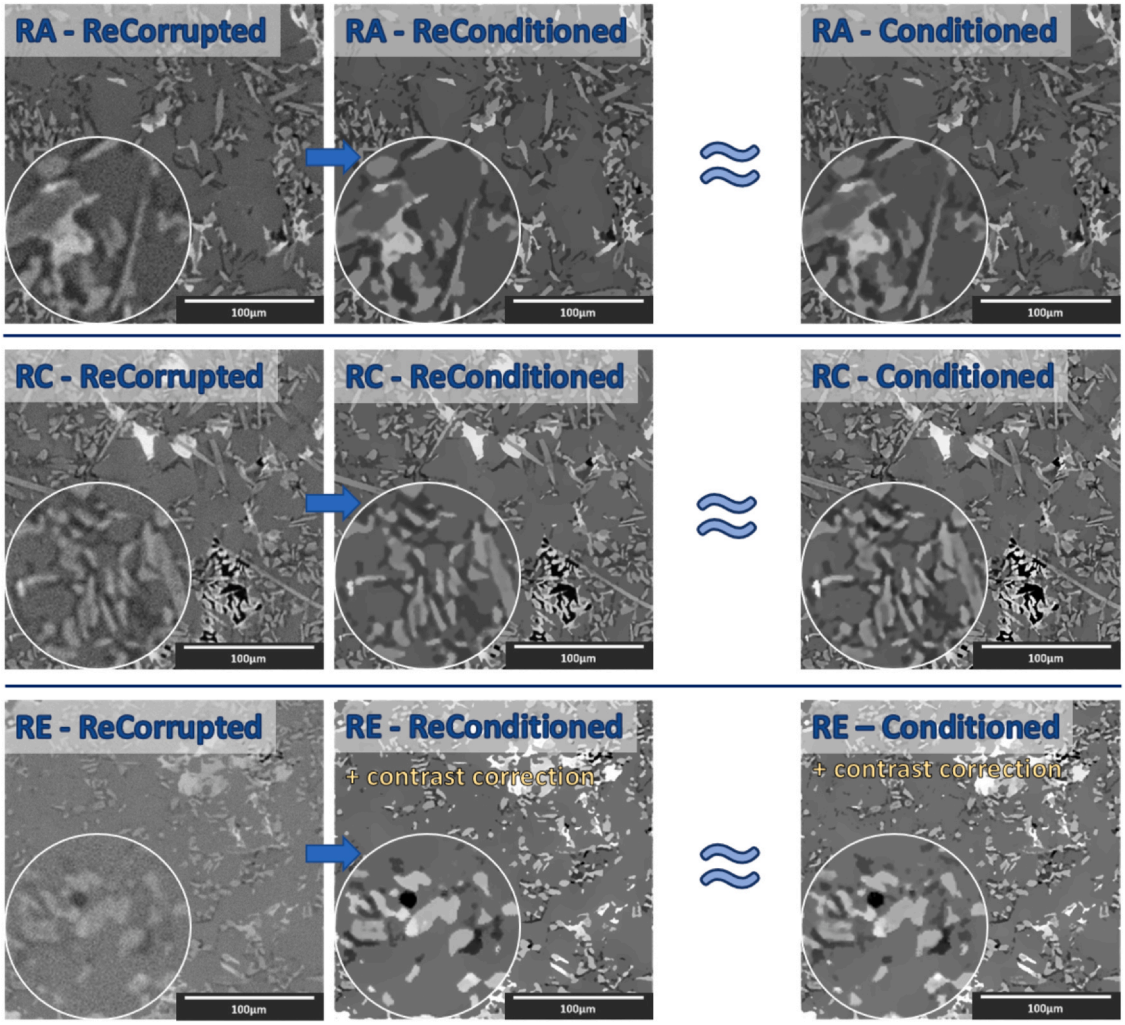

Fig. 17. Previously Conditioned and Re-Conditioned experimental XCT Datasets (RA, RC, and RE).

large drops can be attributed to the limited structural ground-truth grey levels present within the synthetic XCT volumes. On the other hand, in the experimental datasets the structural gray levels are more complex; hence the drop in HE is significantly weakened (especially in group 1, which visually contains the least initial noise). Furthermore, there is a slight increase in the HE values after the deblurring step in all experimental XCT groups: 1–3. This is not unexpected for the reasons previously discussed: deblurring reveals hidden gray levels. However, BM confirms the blur reduction, with the final BM for all datasets being very low between 0.16 and 0.32. The HE and BM drop prove that the suggested framework can also successfully perform on experimental datasets. This can be visually appreciated by observing Fig. 16. Clearly, there is a significant improvement in image quality in terms of noise and blur. Furthermore, we observe the complete elimination of ring artifacts (mainly present in datasets: RA and RE). The performance consistency across datasets belonging to the same group is confirmed by the similar metric patterns. We observe that the metric patterns are, however, not similar across the different data groups. The SSIM metric cannot be employed here to assess the conditioning performance consistency across the different groups, as we do not have ground truth experimental XCT data. Thus, we artificially re-corrupt the conditioned experimental datasets: RA, RC, and RE with simulated blur and noise (1st: mean 3D blurring with sigma = 2, 2nd: Gaussian noise with standard deviation = 9), and then we re-condition them. Cross-sections from the resulting conditioned volumes are illustrated in Fig. 17, revealing that the previously conditioned and re-conditioned images are practically identical. The re-conditioned images appear to have a slightly diminished number of structural gray levels: minor over-conditioning. Some structural deterioration is justifiable due to re-corruption and re-conditioning.

Moreover, as it can be observed in Fig. 18, the HE patterns are essentially identical for the initially conditioned and re-conditioned experimental XCT volumes. The re-conditioned HE values are marginally lower than their previously conditioned equivalents because of the minor over-conditioning. The initial (not yet conditioned XCT datasets) and re-corrupted HE values can significantly differ as we are unaware of the initial noise and blur levels present. However, the similar HE values after the NLM and re-NLM steps essentially prove that the conditioning performance on experimental datasets is consistent irrespective of the initial noise and blur levels. Thus, by inductive reasoning, the overall 92% SSIM conditioning efficiency observed in the case of the synthetic XCT datasets, can also be translated in the case of the experimental XCT datasets. Similarly, the 99% and 95% SSIM conditioning efficiency achieved in the synthetic XCT datasets standalone denoising and standalone deblurring, is translatable to the experimental XCT datasets as well.

Finally, we remark that Tsamos et al. [17] reported that the segmentation performance of a convolutional neural network trained on synthetic materials XCT data is strongly correlated with the quality of the XCT data that are being segmented. Thus, the better the quality of the experimental images is (less noise, less blur, sharp gray-scales transitions between phases without fluctuations, etc.), the more

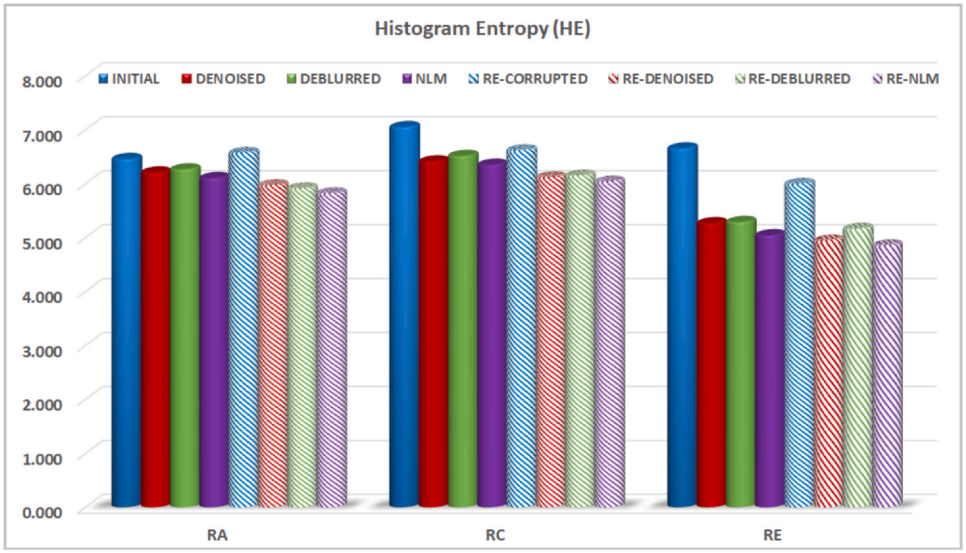

Fig. 18. Resulting HE values of the experimental XCT datasets: RA, RC, and RE, from each step of the conditioning and re-conditioning process.

reliable would be the quantitative information that can be extracted from such images.

6. Conclusions and outlook

A complete multiscale and multilevel conditioning framework was developed: BAM SynthCOND. It consisted of in-house synthetic materials XCT data generation libraries (BAM SynthMAT) [17], in-house designed deep convolutional neural networks (2D/3D ACEnet_Denoise, 2D/3D ACEnet_Deblur) as well as in-house implemented data augmentations, training and forwarding strategies. The proposed multiscale/multilevel conditioning framework for removal of noise and blur in experimental XCT data of complex six-phase Al-Si MMCs performed very well, achieving a consistent overall 92% SSIM efficiency (combined denoising and deblurring), and standalone denoising and deblurring SSIM efficiency: 99% and 95% in post-CT reconstructions, respectively. Moreover, the conditioning allowed also suppressing ring artifacts.

One of the novelties of this work was that the deep convolutional neural networks were trained solely on synthetic XCT data. To our knowledge, there is virtually no public literature on materials XCT data conditioning with deep learning techniques, in which synthetic XCT training data are employed. This strategy allowed circumventing the lack of artifact-free experimental XCT data for supervised training. Another novelty was the introduction of the ACE training strategy which boosts the performance of neural networks trained with continuous loss functions. We also showed that the 2D versions of the proposed networks perform better than their 3D equivalents. In contrast to noise, blur is a geometrically dependent artifact, therefore we believe that a 3D deblurring network can achieve even higher conditioning efficiency if provided with more training data and different training strategies since 2D networks cannot “perceive” the out-of-plane blur. This is left for future work and will be reported in a forthcoming paper.

Another aspect remaining partially open is the quantification of the remaining noise in the final conditioned XCT volumes by means of a metric that is not affected by the number of structural gray levels. In another future publication, we will apply our methods directly on the projections coupled with a standard FBP reconstruction. This should bring a very robust AI-based conditioning tool for CT data as it will rely on the advantages of the superior supervised training. However, conditioning post-CT (reconstructed) datasets with our proposed method can be advantageous for fully automatic segmentation (i.e., no manual annotation of the training data) if the same synthetic data are employed for training the segmentation DCNN.

We believe that the current work is highly interdisciplinary, and thus the methods developed herein can be effortlessly extended to other imaging techniques such as microscopy, thermography, diffraction, and ultrasonics.

Declaration of Competing Interest

The authors declare that they have no known competing financial interests or personal relationships that could have appeared to influence the work reported in this paper.

Acknowledgments

This work has been funded by the BAM-internal Project “Ideen_2019–028″. In memory of Sergei Evsevleev who passed away on November 8th, 2021.

References

[1] H. Lu, X. Li, L. Li, D. Chen, Y. Xing, J. Hsieh, Z. Liang, Adaptive noise reduction toward low-dose computed tomography, SPIE Proc. vol. 5030, (2003), https://doi.org/10.1117/12.480374
[2] J. Hsieh, Adaptive streak artifact reduction in computed tomography resulting from excessive x-ray photon noise, Med. Phys. vol. 25, (11) (1998) 2139–2147, https://doi.org/10.1118/1.598410
[3] I. Mori, Y. Machida, M. Osanai, K. Iinuma, Photon starvation artifacts of X-ray CT: their true cause and a solution, Radiol. Phys. Technol. vol. 6, (1) (2012) 130–141, https://doi.org/10.1007/s12194-012-0179-9
[4] B. Münch, P. Trtik, F. Marone, M. Stampanoni, Stripe and ring artifact removal with combined wavelet - Fourier filtering, Opt. Express vol. 17, (10) (2009) 8567–8591, https://doi.org/10.1364/OE.17.008567
[5] M. Kachelrieß, O. Watzke, W.A. Kalender, Generalized multi-dimensional adaptive filtering for conventional and spiral single-slice, multi-slice, and cone-beam CT, Med. Phys. vol. 28, (4) (2001) 475–490, https://doi.org/10.1118/1.1358303
[6] J. Hsieh, Generalized adaptive median filters and their application in computed tomography, SPIE Proc. vol. 2298, (1994), https://doi.org/10.1117/12.186581
[7] A. Buades, B. Coll, J.-M. Morel, A non-local algorithm for image denoising, 2005 IEEE Comput. Soc. Conf. Comput. Vis. Pattern Recognit. (CVPR’05) vol. 2, (2005) 60–65, https://doi.org/10.1109/cvpr.2005.38
[8] H. Zhang, D. Zeng, H. Zhang, J. Wang, Z. Liang, J. Ma, Applications of nonlocal means algorithm in low-dose X-ray CT image processing and reconstruction: A review, Med. Phys. vol. 44, (3) (2017) 1168–1185, https://doi.org/10.1002/mp.12097
[9] K. Arrell, S. Wise, J. Wood, D. Donoghue, Spectral filtering as a method of visualizing and removing striped artefacts in digital elevation data, Earth Surf. Process. Landf. vol. 33, (6) (2008) 943–961, https://doi.org/10.1002/esp.1597
[10] J. Chen, H. Lin, Y. Shao, L. Yang, Oblique striping removal in remote sensing imagery based on wavelet transform, Int. J. Remote Sens. vol. 27, (2006) 1717–1723, https://doi.org/10.1080/01431160500185516

[11] X. Tang, R. Ning, R. Yu, D. Conover, Cone beam volume CT image artifacts caused by defective cells in x-ray flat panel imagers and the artifact removal using a wavelet-analysis-based algorithm, Med. Phys. (2001), https://doi.org/10.1118/1.1368878
[12] S. Magkos, A. Kupsch, G. Bruno, Direct iterative reconstruction of computed tomography trajectories reconstruction from limited number of projections with DIRECTT, Rev. Sci. Instrum. vol. 91, (10) (2020) 103107, https://doi.org/10.1063/5.0013111
[13] S. Magkos, A. Kupsch, G. Bruno, Suppression of cone-beam Artefacts with Direct Iterative Reconstruction Computed Tomography Trajectories (DIRECTT), J. Imaging vol. 7, (8) (2021) 147–1479, https://doi.org/10.3390/jimaging7080147
[14] K.A.S.H. Kulathilake, N.A. Abdullah, A.Q.M. Sabri, K.W. Lai, A review on deep learning approaches for low-dose computed tomography restoration, Complex Intell. Syst. (2021), https://doi.org/10.1007/s40747-021-00405-x
[15] C. Tang, J. Li, L. Wang, Z. Li, L. Jiang, A. Cai, W. Zhang, N. Liang, L. Li, B. Yan, Unpaired low-dose CT denoising network based on cycle-consistent generative adversarial network with prior image information, Comput. Math. Method Med 2019 (2019) 8639825, https://doi.org/10.1155/2019/8639825
[16] A.A. Hendriksen, D.M. Pelt, K.J. Batenburg, Noise2Inverse: self-supervised deep convolutional denoising for tomography, IEEE Trans. Comput. Imaging 6 (2020) 1320–1335, https://doi.org/10.1109/tci.2020.3019647
[17] A. Tsamos, S. Evsevleev, R. Fioresi, F. Faglioni, G. Bruno, Synthetic data generation for automatic segmentation of X-ray computed tomography reconstructions of complex microstructures, J. Imaging 9 (2) (2023) 22, https://doi.org/10.3390/jimaging9020022
[18] G. Requena, H.P. Degischer, Creep behaviour of unreinforced and short fibre reinforced AlSi12CuMgNi piston alloy, Mater. Sci. Eng. A vol. 1–2, (420) (2006) 265–275, https://doi.org/10.1016/j.msea.2006.01.024
[19] S. Evsevleev, S. Paciornik, G. Bruno, Advanced deep learning-based 3d microstructural characterization of multiphase metal matrix composites, Adv. Eng. Mater. vol. 22, (4) (2020) 1901197, https://doi.org/10.1002/adem.201901197
[20] K.U. Kainer, Metal matrix composites: custom-made materials for automotive and aerospace engineering, Wiley-Vch, Weinheim, 2006.
[21] S. Evsevleev, T. Mishurova, S. Cabeza, R. Koos, I. Sevostianov, G. Garcés, G. Requena, R. Fernandez, G. Bruno, The role of intermetallics in stress partitioning and damage evolution of AlSi12CuMgNi alloy, Mater. Sci. Eng.: A vol. 736, (2018) 453–464, https://doi.org/10.1016/j.msea.2018.08.070
[22] T. Karras, S. Laine, T. Aila, A Style-Based Generator Architecture for Generative Adversarial Networks, IEEE Transactions on Pattern Analysis & Machine Intelligence vol. 43, (2021), pp. 4217–4228 2021.
[23] H. Ren, M. El-Khamy, J. Lee, DN-resnet: efficient deep residual network for image denoising, ACCV (2018), https://doi.org/10.1007/978-3-030-20873-8_14
[24] O. Ronneberger, P. Fischer, T. Brox, U-Net: convolutional networks for biomedical image segmentation, 2015, Lect. Notes Comput. Sci. (2015) 234–241, https://doi.org/10.1007/978-3-319-24574-4_28
[25] P. Ramachandran, B. Zoph, and Q.V. Le, Searching for Activation Functions, arXiv.org (2017). https://arxiv.org/abs/1710.05941.
[26] Neural Network Libraries. An open-source software to make research, development and implementation of neural network more efficient. Sony corp., web: https://nnabla.org/.
[27] D.P. Kingma J. Ba, Adam: A Method for Stochastic Optimization, arXiv.org (2014). https://arxiv.org/abs/1412.6980.
[28] Z. Wang, A.C. Bovik, H.R. Sheikh, E.P. Simoncelli, Image quality assessment: from error visibility to structural similarity, IEEE Trans. Image Process. vol. 13, (4) (2004) 600–612, https://doi.org/10.1109/tip.2003.819861
[29] R.C. Gonzalez, R.E. Woods, S.L. Eddins, Digital Image Processing Using MATLAB, 3rd ed., Prentice Hall, New Jersey, 2003.
[30] H. To, K. Chiang, C. Shahabi, Entropy-based histograms for selectivity estimation, Proc. 22nd ACM Int. Conf. Conf. Inf. Knowl. Manag. - CIKM' 13 (2013), https://doi.org/10.1145/2505515.2505756
[31] F. Crété-Roffet, T. Dolmiere, P. Ladret, M. Nicolas, The blur effect: perception and estimation with a new no-reference perceptual blur metric, Proc. SPIE 6492 - Hum. Vis. Electron. Imaging XII (2007), https://doi.org/10.1117/12.702790
[32] P. Ndajah, H. Kikuchi, M. Yukawa, H. Watanabe, S. Muramatsu, An investigation on the quality of denoised images, International Journal of Circuits, Systems and Signal Processing, Int. J. Circuit. Syst. Signal Process. vol. 5, (4) (2011) 423–434.
[33] E. Hariyanto, A.P. Utama Siahaan, S. Aryza, Experimental study of modified multilevel median filter for noise reduction, Int. J. Sci. Res. Sci. Technol. (2019) 135–139, https://doi.org/10.32628/ijsrst196123
[34] Erwin, A. Nevriyanto, D. Purnamasari, Image enhancement using the image sharpening, contrast enhancement, and Standard Median Filter (Noise Removal) with pixel-based and human visual system-based measurements, IEEE Xplore (2017), https://doi.org/10.1109/ICECOS.2017.8167116
[35] Y. Liu, A method of CT image denoising based on residual encoder-decoder network, J. Healthc. Eng. (2021), https://doi.org/10.1155/2021/2384493
[36] T.A. Mahmoud, S. Marshall, Edge-detected guided morphological filter for image sharpening, EURASIP J. Image Video Process. (2008) 1–9, https://doi.org/10.1155/2008/970353